PRODUCTION ENGINEERING ARCHIVES 2025, 31(4), 534-549

PRODUCTION ENGINEERING ARCHIVES

ISSN 2353-5156 (print)
ISSN 2353-7779 (online)

Exist since 4th quarter 2013
Available online at https://pea-journal.eu

Statistical optimization and microstructural insights into roller burnishing of BMD 316L stainless steel

Krittanun Santiwongsagorn[1], **Chanerin Ruksut**[1], **Suthiwat Waewdee**[1], **Phanphong Kongphan**[1*]

[1] Department of Industrial Engineering, Faculty of Engineering, Rajamangala University of Technology Thanyaburi, Thanyaburi, Pathum Thani 12110, Thailand; krittanun_s@mail.rmutt.ac.th (KS); chanerin.r@en.rmutt.ac.th (CR); suthiwat_w@mail.rmutt.ac.th (SW); phanphong.k@en.rmutt.ac.th (PK)
*Correspondence: phanphong.k@en.rmutt.ac.th

Article history
Received 27.08.2025
Accepted 05.11.2025
Available online 12.12.2025

Keywords
Roller burnishing,
Bound Metal Deposition (BMD),
AISI 316L stainless steel,
Response Surface Methodology (RSM),
Surface integrity.

Abstract
Bound Metal Deposition (BMD) is a cost-effective additive manufacturing process, but BMD-fabricated AISI 316L stainless steel often suffers from high surface roughness, residual porosity, and low hardness, which limits its fatigue and wear resistance. This study presents the first systematic optimization of roller burnishing for BMD 316L, combining experimental evaluation, statistical modelling, and microstructural characterization. Unlike Laser Powder Bed Fusion (LPBF) steels, where burnishing modifies melt-pool patterns, improvements in BMD arise from pore closure and strain hardening of a sintered microstructure. A Central Composite Design under Response Surface Methodology (RSM) evaluated the effects of cutting speed, feed rate, and penetration depth on surface roughness (Ra) and hardness (HV0.1). ANOVA identified feed rate as the dominant factor for roughness ($p < 0.001$), while penetration depth governed hardness ($p < 0.001$); cutting speed showed no significant effect. Quadratic models achieved strong predictive accuracy (R^2 = 89.9% for Ra, 84.0% for HV). Optimization predicted Ra = 1.679 µm and HV = 301.9, validated experimentally (Ra = 1.643 µm, HV = 308). Microstructural and EBSD analyses confirmed asperity deformation, partial pore closure, and grain refinement, producing a hardened layer of ~1.0–1.2 mm. These results demonstrate roller burnishing as a geometry-preserving, cost-effective finishing route for BMD steels, with future work required to validate fatigue and wear performance.

DOI: 10.30657/pea.2025.31.50

1. Introduction

Additive Manufacturing (AM), or 3D printing, is widely regarded as a transformative technology of the Fourth Industrial Revolution (Industry 4.0), enabling direct production of complex components from digital models with benefits in design freedom, material efficiency, and decentralized production (Gao et al., 2015; Xiang et al., 2024). AM has impacted aerospace, biomedical, automotive, and energy sectors, supporting lightweight structures, customized implants, and sustainable production (Ford & Despeisse, 2016; Frazier, 2014; Ngo et al., 2018). Among various processes such as Powder Bed Fusion (PBF), Directed Energy Deposition (DED), and extrusion-based methods (Armstrong et al., 2022), Bound Metal Deposition (BMD) has emerged as a cost-effective and office-friendly technique. BMD employs metal-polymer rods extruded layer by layer into "green parts," followed by debinding and sintering, eliminating lasers and powders while maintaining broad alloy compatibility (Gabilondo et al., 2022).

Despite these advantages, BMD parts often contain sintering-related porosity (~5%), anisotropy, shrinkage, and high surface roughness that reduce mechanical performance compared to PBF alloys (Basak et al., 2024; Gonzalez-Gutierrez et al., 2018; Saboori et al., 2020). Optimizing build parameters improves density and strength (Basak et al., 2024; Gabilondo et al., 2022), yet surface roughness typically exceeds 20 µm Ra, impairing dimensional accuracy, fatigue life, and wear resistance (Afkhami et al., 2021; D'Andrea, 2023; Kurdi et al., 2023; Yildiz, Ozdogan, & Malekan, 2024). Thus, effective post-processing is required to improve surface integrity and reliability of BMD stainless steels.

Post-processing methods for AM include mechanical, thermal, and chemical approaches (Bello et al., 2023; Malakizadi et al., 2022). Thermal treatments such as HIP improve density but are costly and geometry-limited (Ge et al., 2023; Teschke et al., 2022). Chemical polishing achieves smooth finishes but struggles with complex geometries (Bello et al., 2023). Mechanical methods such as grinding and polishing improve roughness but risk altering near-net-shape geometries (Karthick Raaj et al., 2020; Rotella et al., 2020). In contrast, roller burnishing plastically deforms asperities, induces compressive residual stresses, and increases hardness without material removal (Rotella et al., 2020; Sanguedolce et al., 2022). Burnishing has improved fatigue life and wear resistance in LPBF 316L (Davoodi et al., 2023; Duncheva et al., 2024; Sayadi et al., 2023), but mechanisms differ from BMD due to the latter's sintering-induced porosity and coarser microstructure (Saboori et al., 2020).

Recent studies have further shown that advanced roller burnishing techniques, such as Slide Roller Burnishing (SRB) and Ultrasonic Rolling (UR), substantially improve fatigue life and surface integrity in LPBF and LDED alloys by redistributing residual stresses, refining solidification structures, and reducing defect sensitivity (Duncheva et al., 2024; Liu et al., 2024; Maximov et al., 2024). However, these mechanisms differ fundamentally from those in BMD steels, where pore closure and strain hardening of sintered microstructures dominate instead of melt-pool refinement. This distinction underlines the need for roller burnishing parameter strategies specifically tailored for BMD, since process effectiveness relies on different strengthening pathways compared with LPBF/DED alloys.

To date, research on roller burnishing has largely focused on LPBF and other fusion-based AM alloys (Rodriguez et al., 2020; Rotella et al., 2020; Sanguedolce et al., 2022; Sayadi et al., 2023), leaving binder-based routes such as BMD underexplored. In particular, systematic parameter optimization has not been reported. To the best of our knowledge, this is the first study to develop and validate a Response Surface Methodology (RSM) framework for roller burnishing applied specifically to BMD stainless steel. By integrating statistical modeling with microstructural and EBSD analyses, this work provides mechanistic insight and predictive guidelines to enhance surface integrity of BMD 316L, addressing a critical gap in the literature.

2. Literature review

Post-processing is critical for improving the performance of additively manufactured (AM) parts, with available approaches categorized into mechanical, thermal, and chemical treatments (Bello et al., 2023; Malakizadi et al., 2022). Mechanical methods such as shot peening, grinding, polishing, and burnishing correct surface defects through plastic deformation or abrasion. Shot peening induces compressive residual stresses that improve fatigue resistance but risks overpeening and limited coverage (Okuniewski et al., 2024; Sayadi et al., 2023). Grinding and polishing effectively reduce roughness but may compromise dimensional accuracy, which is especially critical for near-net-shape AM parts (Karthick Raaj et al., 2020; Rotella et al., 2020).

Thermal post-processing, such as Hot Isostatic Pressing (HIP) and heat treatments, reduces porosity and homogenizes microstructures. HIP can lower porosity below 0.01%, substantially extending fatigue life, but is costly and limited by component geometry (Ge et al., 2023; Teschke et al., 2022). Heat treatments improve bulk mechanical properties but exert limited influence on surface finish. Chemical methods, including chemical and electrochemical polishing, can achieve very smooth surfaces but are restricted to accessible geometries and require complex chemical handling (Bello et al., 2023).

By contrast, roller burnishing offers unique advantages: it can be applied in situ without material removal, preserves near-net-shape geometry, induces compressive residual stresses, and enhances hardness (Rotella et al., 2020; Sanguedolce et al., 2022). These benefits are particularly valuable for AM components, where surface defects and porosity strongly affect performance (Sayadi et al., 2023). Several studies confirm burnishing's value for AM stainless steels: fatigue life of LPBF 316L increased from $\sim 1.35\times10^5$ to $>3.03\times10^6$ cycles (Sayadi et al., 2023), and surface roughness and wear resistance improved through asperity smoothing and residual stress redistribution (Davoodi et al., 2023; Duncheva et al., 2024). Process parameters such as force, feed, roller geometry, number of passes, and lubrication strongly influence outcomes (Noronha et al., 2024; Priyadarsini, Venkata et al., 2019).

However, the mechanisms of roller burnishing differ between AM processes. In Laser Powder Bed Fusion (LPBF), improvements arise primarily from flattening melt-pool solidification patterns and redistributing residual stresses in a fine cellular microstructure (Davoodi et al., 2023; Sayadi et al., 2023). By contrast, Bound Metal Deposition (BMD) produces components with sintering-induced porosity, particle-boundary heterogeneities, and coarser grains (Basak et al., 2024; Saboori et al., 2020).

Basak et al. (2024) systematically characterized BMD 316L and reported apparent densities ranging from 79 to 97 % of theoretical, depending on nozzle diameter, infill density, and layer thickness. Residual porosity of 3–6 % was mainly observed as unmelted spots, incomplete fusion zones, and triple-junction pores. The study also highlighted anisotropic tensile behavior, with horizontally built specimens exhibiting ~160 MPa higher UTS than vertically built ones due to differences in void distribution and interlayer bonding. These findings underscore the inherent porosity and anisotropy of BMD steels, which limit their mechanical performance relative to cast or LPBF alloys. Thus, while LPBF burnishing mechanisms are linked to melt-pool smoothing, improvements in BMD are expected to result from localized pore closure, densification, and strain hardening in the plastically deformed near-surface layer. This distinction underscores the need for dedicated studies of BMD rather than extrapolation from LPBF results.

Despite progress in binder-based AM research, most investigations have focused on build parameters and sintering outcomes rather than post-processing. Gonzalez-Gutierrez et al. (2018) reviewed extrusion-based routes, highlighting challenges with porosity and shrinkage. Gabilondo et al. (2022) demonstrated how build orientation, chamber temperature, and infill affect BMD 316L strength, while Basak et al. (2024) linked nozzle diameter and infill density to densification and microstructural evolution. These studies confirm the unique defect origins of BMD but do not examine finishing processes.

In summary, while roller burnishing has been widely shown to enhance the surface finish, hardness, and fatigue resistance of LPBF stainless steels (Davoodi et al., 2023; Duncheva et al., 2024; Sayadi et al., 2023), its mechanisms are not directly transferable to BMD components, which are dominated by sintering-induced porosity, particle-boundary heterogeneities, and coarser grains (Basak et al., 2024; Saboori et al., 2020). Binder-based AM studies (Basak et al., 2024; Gabilondo et al., 2022; Gonzalez-Gutierrez et al., 2018) have primarily addressed densification, build parameters, and sintering behavior, but have not examined finishing processes or parameter optimization. This study addresses these gaps by presenting the first systematic optimization of roller burnishing for BMD-fabricated AISI 316L stainless steel. Using Response Surface Methodology (RSM), the effects of cutting speed, feed rate, and penetration depth are statistically evaluated, while microstructural and EBSD analyses provide mechanistic explanations of asperity deformation, pore closure, and grain refinement. Together, these contributions establish a predictive and experimentally validated framework tailored specifically to the unique microstructure and defects of BMD stainless steel.

3. Experimental

3.1. Experimental specimens

Cylindrical AISI 316L specimens (Fig. 1) were produced via BMD (Studio System 2, Desktop Metal, USA). Filaments composed of alloy powders and polymer binders were deposited layer-by-layer into "green parts," followed by debinding and sintering in a high-temperature atmosphere to achieve densification. Unlike PBF, BMD offers lower facility requirements and greater safety as it avoids lasers and powders.

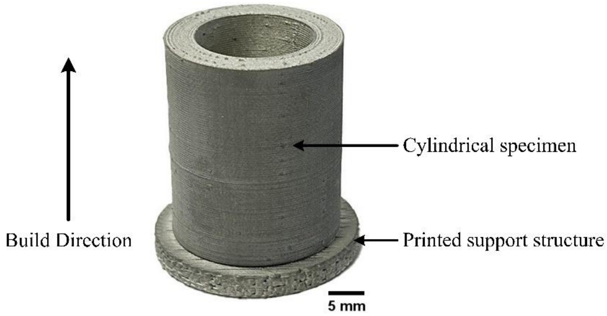

Fig. 1. Cylindrical AISI 316L specimen fabricated by the BMD process. The arrow indicates the build direction, and the support structure is shown at the base.

Specimens were designed with an outer diameter of 25 mm, inner diameter of 17 mm, and length of 30 mm, reaching 96–99% of theoretical density (8.00 g/cm³). Chemical composition is shown in Table 1, with BMD printing and sintering parameters in Tables 2 and 3. Feedstock chemistry matched 316L (UNS S31603 / EN 1.4404), including Ni = 10–13 wt%, which is compliant for sinter-based AM routes such as BMD; note that the 13–15 wt% Ni range pertains to implant-grade 316L/316LVM (ISO 5832-1) and is not applicable here. Dimensional accuracy and properties are summarized in Table 4.

Table 1. Chemical composition of AISI 316L stainless steel used in this study.

Element	Content (wt%)
Chromium (Cr)	16.5–18.5
Nickel (Ni)	10–13
Molybdenum (Mo)	2.0–2.5
Manganese (Mn)	≤ 2.00
Silicon (Si)	≤ 0.03
Carbon (C)	≤ 0.03
Phosphorus (P)	≤ 0.04
Nitrogen (N)	≤ 0.10
Iron (Fe)	Balance (~60–70)

Table 2. BMD printing parameters used in this study.

Parameter	Value
Layer thickness	200 μm
Nozzle diameter	0.4 mm
Printing speed	30–50 mm/s
Infill density	100%
Printing temperature	220–230°C
Printing atmosphere	Ambient air
Bed temperature	60°C

Table 3. BMD sintering parameters used in this study.

Parameter	Value
Sintering temperature	1360°C
Holding time	2 h
Heating rate	0.2°C·min^{-1}
Cooling rate	Furnace cooling
Atmosphere	Partial-pressure sintering

Table 4. Dimensions and properties of the BMD-fabricated specimens.

Dimension	Average	Std. Dev.
Outer diameter (mm)	25.01	0.34
Inner diameter (mm)	16.98	0.30
Total length (mm)	29.95	0.46
Surface roughness, Ra (μm)	21.3	3.60
Hardness (HV0.1)	129	9.85

Table 4 shows the specimens retained dimensional accuracy within 1% of CAD values, comparable to other binder-based AM routes (Kedziora et al., 2022). However, average surface roughness was high (21.3 ± 3.6 μm Ra), reflecting the staircase effect typical of extrusion-based AM. This is rougher than as-built LPBF parts (10–30 μm Ra), which can be polished to <6 μm or even 1–2 μm (Yildiz et al., 2024). Hardness averaged 129 HV0.1, consistent with sintered BMD/FFF alloys (120–150 HV), but lower than LPBF 316L (200–253 HV) due to coarser microstructures and residual porosity (Afkhami et al., 2021; D'Andrea, 2023; Kurdi et al., 2023). BMD yields near-net-shape parts with good dimensional control but requires post-processing to address rough surfaces and lower hardness.

3.2. Roller burnishing tool

The tool (Fig 2) comprised a hardened JIS SKD 11 steel roller (58–60 HRC, 50 mm diameter, 5 mm radius) mounted in custom holders on precision angular contact bearings (NSK 6900-ZZ). The roller shaft was made from JIS SCM440 alloy steel with an interference fit to ensure concentricity and minimize runout. This robust assembly ensured stable pressure application.

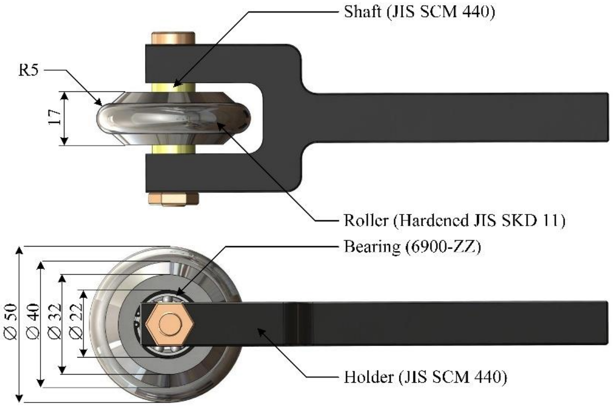

Fig 2. Schematic of the roller burnishing tool used in this study, showing the roller, holder, bearing, and shaft assembly (all dimensions in mm).

3.3. Experimental set-up

Experiments were conducted on a CNC lathe (Nexus 150 II, Mazak, Japan). Specimens were mounted between centers with torque transmitted by a lathe dog for accurate alignment. The roller tool contacted the outer surface and rotated freely under applied feed and penetration, plastically deforming asperities (Fig. 3).

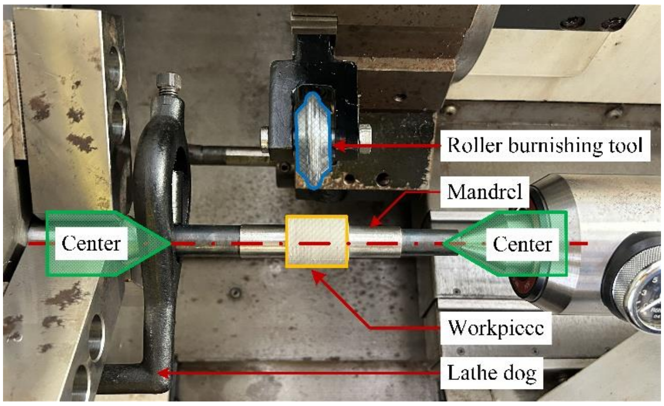

Fig. 3. Experimental set-up of the roller burnishing process, showing the roller burnishing tool, cylindrical workpiece, and supporting fixtures (lathe dog, mandrel, and centers).

Before each run, the roller was cleaned and coated with cutting oil (246-R, Miyagawa, Japan) to reduce friction and prevent adhesion. Lubrication stabilizes pressure, distributes stresses uniformly, and improves plastic deformation, reducing tool wear and surface damage, (Grudzień et al., 2024; Kalisz et al., 2021). Dry burnishing, by contrast, increases heating and instability (Bobrovskij et al., 2022; Low & Wong, 2011). Strict cleaning and lubrication ensured reproducible results (Boudjerada & Ghochi, 2024).

3.4. Design of Experiments (DOE)

The experiment was structured using a Central Composite Design (CCD) within the framework of Response Surface Methodology (RSM) to investigate the influence of key process parameters on surface quality and mechanical response. As summarized in Table 5, three factors were considered: cutting speed (A), feed rate (B), and depth of penetration (C) – selected based on their documented influence on surface finish and mechanical properties in roller burnishing processes. Each factor was varied across five levels, corresponding to the axial points (−α, +α), factorial points (−1, +1), and the centre point (0). This design enabled comprehensive exploration of the parameter space, allowing both linear and quadratic effects to be modelled for statistical optimization.

A rotatable three-factor, five-level CCD comprising 17 distinct design points was employed, and each condition was conducted in triplicate (n = 3) to evaluate repeatability and provide an estimate of pure error. In total, 51 experimental runs were performed under identical setup conditions and arranged in a completely randomized order generated by Minitab® 18 (Minitab LLC, USA) to minimize systematic bias from potential time-dependent effects such as tool wear or temperature variation. All statistical analyses were conducted at a significance level of $\alpha = 0.05$.

Table 5. Experimental factors, responses, and optimization objectives used in the Central Composite Design (CCD).

Factors	Unit	Level				
		-α	Low (-1)	Center (0)	High (+1)	+α
Cutting speed (A)	$m \cdot min^{-1}$	44.55	65	95	125	145.45
Feed rate (B)	$mm \cdot rev^{-1}$	0.032	0.1	0.2	0.3	0.368
Depth of penetration (C)	mm	0.132	0.2	0.3	0.4	0.468
	Responses		Unit		Statistical target	
	Surface roughness (Ra)		µm		Minimized	
	Surface hardness (HV0.1)		HV0.1		Maximized	

Note: Statistical testing was conducted at a significance level of $\alpha = 0.05$.

The selected cutting speed range (44.55–145.45 $m \cdot min^{-1}$) was informed by previous studies on AISI 316L and similar alloys. For example, Samir et al. (2018) and Maximov & Duncheva (2024) reported effective burnishing speeds in the range of 25 to 150 m/min during process optimization for surface roughness and hardness improvement. Similarly, the feed rate was varied from 0.032 to 0.368 $mm \cdot rev^{-1}$, aligning with prior research indicating optimal ranges between 0.05 and 0.3 mm/rev for favorable surface responses (Nguyen et al., 2024; Rotella et al., 2020).

The depth of penetration (0.132–0.468 mm) was selected as a surrogate for applied compressive pressure. This choice was made due to its greater practicality in experimental control, lower equipment requirements, and well-documented ability to govern surface stress profiles. El-Khabeery and El-Axir (2001) and Vukelic et al. (2013) emphasized the convenience and reliability of penetration depth as a controlling parameter in roller burnishing trials. Nguyen et al. (2024) further validated that penetration depth significantly influenced energy-force efficiency and surface outcomes, while studies by Rotella et al. (2020) and Teimouri & Amini (2019) confirmed that changes in depth directly affect residual stress distribution and strain behavior. Additionally, Li et al. (2012) demonstrated that surface roughness and plastic deformation can be reliably predicted when penetration depth is used as the principal control input.

Although penetration depth was employed as the surrogate for contact pressure in this study, it is acknowledged that in situ force measurement would provide a more direct quantification of the applied stresses. Several prior works (Rotella et al., 2020; Teimouri & Amini, 2019) have shown a strong correlation between penetration depth and contact load, supporting the present approach. Nevertheless, future work should incorporate load cells or dynamometers to validate the penetration–pressure relationship under BMD-specific conditions and further enhance process generalizability.

Two response variables were measured to evaluate process performance: surface roughness (Ra), expressed in micrometers (μm), and surface hardness (HV0.1). The optimization objective was to minimize Ra while maximizing hardness, reflecting the dual aim of achieving smoother surfaces with enhanced mechanical properties. Statistical testing was carried out at a significance level ofα = 0.05 to ensure the reliability of results.

3.5. Measuring methods

To evaluate the effectiveness of the roller burnishing process defined in the DOE (Section 3.4), two response variables were measured: surface roughness (Ra) and surface hardness (HV0.1). These parameters were selected to capture both the geometric and mechanical aspects of surface integrity. Ra reflects the efficiency of asperity flattening and material flow on the cylindrical surface, while HV0.1 represents subsurface strengthening associated with plastic deformation and compressive stress induction.

Both measurements were conducted on the specimens before and after the burnishing process, enabling direct comparison of the improvement achieved under varying combinations of cutting speed, feed rate, and depth of penetration. Together, Ra and HV0.1 provide a comprehensive assessment of burnishing effectiveness, aligning with the optimization objectives of minimizing roughness and maximizing hardness.

3.5.1. Surface roughness measurement

Surface roughness (Ra) was measured on the outer cylindrical surface of the specimen, which was directly in contact with the burnishing roller. A surface roughness tester (CV-3000, Mitutoyo, Japan) was used in accordance with ISO 4287, configured with a cutoff length of 0.8 mm and an evaluation length of five cutoff lengths.

For each specimen, three measurements were taken at different axial positions (Fig. 4), and the mean value was recorded to reduce local variability and ensure representative results.

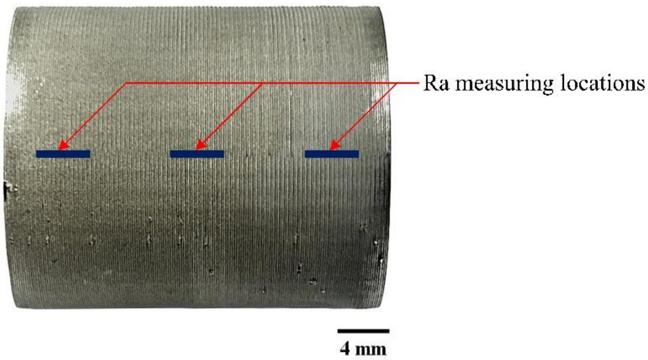

Fig. 4. Axial positions selected for surface roughness (Ra) measurements on the outer cylindrical surface.

Ra, expressed as the arithmetic mean deviation from the mean line, is widely used in machining and burnishing research because it correlates with key functional properties such as friction, wear, and lubrication, while ensuring comparability with prior studies (Cobanoglu & Ozturk, 2014; Ferencsik et al., 2016; Somatkar et al., 2024).

3.5.2. Surface hardness measurements

Surface hardness measurements were conducted to evaluate the enhancement in hardness and wear resistance induced by the roller burnishing process. A Vickers hardness tester (MXT70, Matsuzawa, Japan) was used in accordance with ASTM E92-17 and ISO 6507-1: 2008. The testing parameters are summarized in Table 6.

Indentations were performed with a 100 gf load and 15 s dwell time along three radial lines spaced 120° apart on the cross-section of each specimen. The indentation spacing progressively increased from 80 μm near the surface to 1000 μm toward the core, giving a final depth of ≈ 2.44 mm (Fig. 5). This approach enabled depth-resolved evaluation of the hardness profile, providing insight into the extent of surface strengthening achieved by roller burnishing.

Table 6. Testing conditions for Vickers surface hardness measurement.

Parameter	Specification
Test load	100 gf
Dwell time	15 s
Measurement lines	3 radial lines spaced 120° apart on the specimen cross-section
Indentation spacing	80, 80, 80, 100, 400, 700, and 1000 μm from the specimen surface (progressive)
Indentations per line	7
Total indentations	21 per specimen

In accordance with ASTM E92-17 and ISO 6507-1:2018, hardness values were averaged from multiple impressions and reported as whole numbers, since the measurement uncertainty typically exceeds 1 %. When uncertainty is below 1 %, one decimal place may be used. For clarity of data distribution, the range (minimum–maximum) of hardness values was also included. Decimal values greater than 0.5 were rounded to the nearest integer following ASTM E29 (Practice for Using Significant Digits).

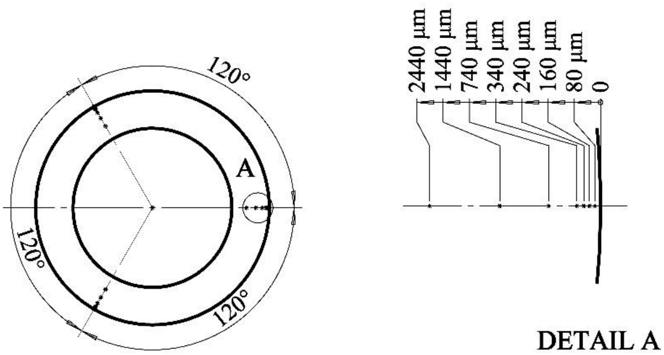

Fig. 5. Schematic of hardness measurement locations on the polished cross-section of the specimen.

3.5.3. Microstructural Analysis

Microstructural analysis was performed to assess the surface integrity and subsurface modifications induced by roller burnishing in AISI 316L specimens. Both conventional and advanced microscopy techniques were employed to characterize grain morphology, crystallographic features, and potential defects. Optical Microscopy (OM) (BH-2, Olympus, Japan) was used as a preliminary method to evaluate overall surface quality, grain morphology, and the presence of porosity, microcracks, or other surface irregularities. This technique provided a general overview of the effects of mechanical deformation on the near-surface region. For detailed crystallographic characterization, Scanning Electron Microscopy (SEM) (SU8230, Hitachi High-Tech Corporation, Japan) combined with Electron Backscatter Diffraction (EBSD) (Symmetry S3, Oxford Instruments, UK) was applied in accordance with ASTM E2627-13. This approach enabled examination of grain orientation, crystallographic texture, and the degree of grain refinement and sub-grain formation resulting from plastic deformation. Together, OM and SEM–EBSD offered complementary insights into both the morphological and crystallographic responses of the material, providing a comprehensive evaluation of surface and subsurface integrity after burnishing.

It is acknowledged that penetration depth was employed in this study as a surrogate for contact pressure due to its practicality and widespread use in roller burnishing research (El-Khabeery & El-Axir, 2001; Vukelic et al., 2013). Although this approach has been validated in prior studies, in-situ force measurement (e.g., using load cells or dynamometers) would provide a more direct quantification of applied stresses and should be pursued in future work to strengthen process generalizability. In addition, all verification trials were conducted on specimens fabricated within the same BMD production batch to minimize uncontrolled variation. While this ensured internal consistency, BMD is known to exhibit batch-to-batch variability arising from sintering shrinkage and porosity distribution. Future work should therefore extend repeatability testing across multiple builds to confirm the robustness of the optimization framework.

4. Results and discussion

4.1. Experimental results

The experimental matrix and measured responses of surface roughness and hardness are presented in Table 7. Statistical models were developed using a quadratic response surface framework, and their adequacy was assessed through ANOVA, R^2 values, and residual analysis

In addition, Table 8 presents averaged responses with standard deviations, 95 % confidence intervals, and partial effects (ΔRa, ΔHV), derived from three replications per condition, providing a clear basis for subsequent regression and trend analysis.

Table 7. Experimental design matrix and measured responses.

Factors			Responses								
A	B	C	Run	Roughness (µm)	Hardness (HV0.1)	Run	Roughness (µm)	Hardness (HV0.1)	Run	Roughness (µm)	Hardness (HV0.1)
65	0.1	0.2	1	1.94	205	18	2.40	163	35	2.92	179
125	0.1	0.2	2	2.19	190	19	1.62	163	36	2.59	150
65	0.3	0.2	3	4.96	213	20	5.42	191	37	5.02	172
125	0.3	0.2	4	4.10	200	21	5.21	178	38	4.79	159
65	0.1	0.4	5	2.67	263	22	2.38	246	39	1.85	246
125	0.1	0.4	6	2.00	267	23	2.39	258	40	2.04	245
65	0.3	0.4	7	4.55	251	24	4.11	271	41	4.44	248
125	0.3	0.4	8	4.25	285	25	5.03	276	42	5.43	271
44.55	0.2	0.3	9	4.07	208	26	3.20	246	43	3.70	236
145.45	0.2	0.3	10	3.57	204	27	3.99	217	44	3.66	203
95	0.032	0.3	11	1.67	239	28	1.01	245	45	1.36	232
95	0.368	0.3	12	5.58	198	29	4.90	209	46	5.04	206
95	0.2	0.132	13	4.31	133	30	3.69	151	47	3.23	164
95	0.2	0.468	14	4.26	310	31	3.91	289	48	3.21	269
95	0.2	0.3	15	3.30	209	32	3.81	210	49	3.48	183
95	0.2	0.3	16	3.25	237	33	2.64	214	50	3.07	177
95	0.2	0.3	17	3.10	230	34	3.98	221	51	3.31	185

Note: Factor A = Cutting speed ($m \cdot min^{-1}$), Factor B = Feed rate ($mm \cdot rev^{-1}$), and Factor C = Depth of penetration (mm).

Table 8. Experimental conditions with averaged responses (n = 3), including standard deviation (SD), 95% confidence intervals (CI), and partial effects. ΔRa = 21.3 − Rā (reduction in surface roughness relative to as-built), ΔHV = HV̄ − 129 (increase in hardness relative to as-built).

Run	A	B	C	Rā (μm)	SD (Ra)	95% CI (Ra)	HV̄ (HV0.1)	SD (HV)	95% CI (HV)	ΔRa (μm)	ΔHV (HV0.1)
1,18,35	65.00	0.10	0.20	2.42	0.49	[1.20–3.64]	183	21.2	[130 – 235]	18.88	54
2,19,36	125.00	0.10	0.20	2.13	0.49	[0.92–3.34]	168	20.4	[117 – 218]	19.17	39
3,20,37	65.00	0.30	0.20	5.13	0.25	[4.51–5.75]	192	20.52	[141 – 243]	16.17	63
4,21,38	125.00	0.30	0.20	4.70	0.56	[3.31–6.09]	179	20.52	[128 – 230]	16.6	50
5,22,39	65.00	0.10	0.40	2.30	0.42	[1.27–3.33]	252	9.81	[227 – 276]	19	123
6,23,40	125.00	0.10	0.40	2.14	0.21	[1.61–2.68]	256	11.06	[229 – 284]	19.16	127
7,24,41	65.00	0.30	0.40	4.37	0.23	[3.80–4.94]	257	12.5	[226 – 288]	16.93	128
8,25,42	125.00	0.30	0.40	4.90	0.6	[3.41–6.39]	277	7.09	[260 – 295]	16.4	148
9,26,43	44.55	0.20	0.30	3.66	0.44	[2.57–4.74]	230	19.7	[181 – 279]	17.64	101
10,27,44	145.45	0.20	0.30	3.74	0.22	[3.19–4.29]	208	7.81	[189 – 227]	17.56	79
11,28,45	95.00	0.032	0.30	1.35	0.33	[0.53–2.17]	239	6.51	[223 – 255]	19.95	110
12,29,46	95.00	0.368	0.30	5.17	0.36	[4.28–6.07]	204	5.69	[190 – 218]	16.13	75
13,30,47	95.00	0.20	0.132	3.74	0.54	[2.40–5.09]	149	15.57	[111 – 188]	17.56	20
14,31,48	95.00	0.20	0.468	3.79	0.53	[2.47–5.12]	289	20.5	[238 – 340]	17.51	160
15,32,49	95.00	0.20	0.30	3.53	0.26	[2.89–4.17]	200	15.31	[163 – 239]	17.77	71
16,33,50	95.00	0.20	0.30	2.99	0.41	[1.98–4.01]	209	30.27	[134 – 285]	18.31	80
17,34,51	95.00	0.20	0.30	3.46	0.34	[2.62–4.29]	212	23.81	[153 – 271]	17.84	83

4.1.1. Surface Roughness (Ra, µm)

Surface roughness values varied widely, ranging from 1.01 µm (Run 28) to 5.58 µm (Run 12). The lowest roughness was achieved at low feed rates combined with moderate penetration depths, while the highest occurred at the maximum feed rate (0.368 mm·rev^{-1}).

Residual diagnostics confirmed model adequacy (Fig. 6).

The normal probability plot indicated data normality (p = 0.640), residuals versus fitted values showed random scatter (homoscedasticity), and residuals versus order confirmed independence. These results support the use of ANOVA for model validation. ANOVA results (Table 9) revealed that the quadratic model was highly significant ($p < 0.001$). Among the linear factors, feed rate was the only statistically significant term ($p < 0.001$), contributing the largest share of variance (Sum of Squares = 59.37; F = 349.29). Cutting speed (p = 0.662) and penetration depth (p = 0.426) were not significant within the tested range.

Quadratic and interaction terms showed comparatively small effects. Only the quadratic term of penetration depth approached significance (p = 0.057), suggesting the possibility of non-linear effects at higher penetration levels. All other squared and interaction terms were not significant ($p > 0.05$).

The main and interaction effects in (Fig. 7) confirm that feed rate is the dominant parameter influencing surface roughness. Increasing the feed rate markedly raised Ra, whereas variations in cutting speed and penetration depth had comparatively minor effects. The nearly parallel interaction lines indicate weak coupling among variables, with only slight divergence at high feed and deep penetration – suggesting limited synergistic interaction.

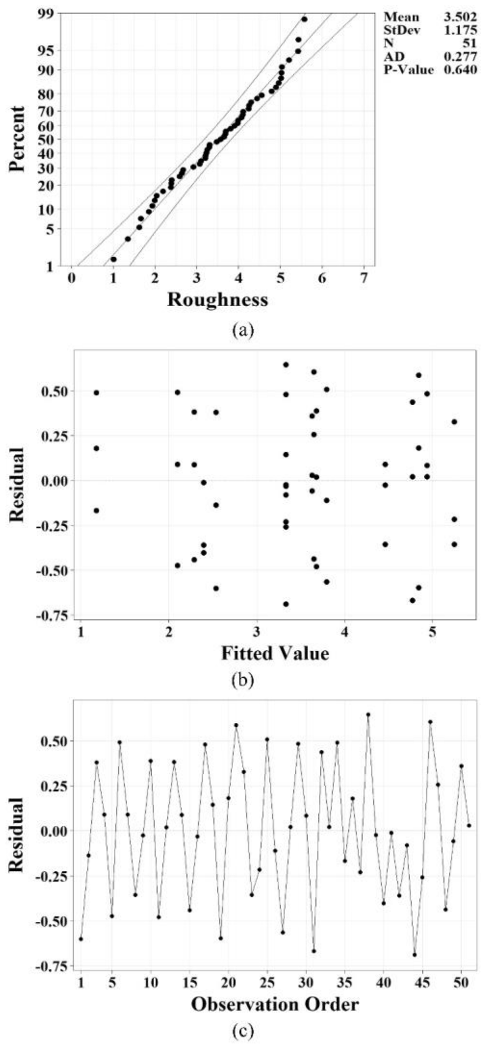

Fig. 6. Statistical analysis of surface roughness (a) Normal probability plot, (b) Residual versus fitted value, and (c) Residual versus order.

Table 9. Analysis of variance of surface roughness response.

Source	DF	Adj SS	Adj MS	F-Value	P-Value
Model	9	62.0977	6.8997	40.60	0.000
Linear	3	59.5097	19.8366	116.71	0.000
Cutting speed	1	0.0330	0.0330	0.19	0.662
Feed rate	1	59.3670	59.3670	349.29	0.000
Depth of penetration	1	0.1097	0.1097	0.65	0.426
Square	3	1.2335	0.4112	2.42	0.080
Cutting speed*Cutting speed	1	0.4415	0.4415	2.60	0.115
Feed rate*Feed rate	1	0.0581	0.0581	0.34	0.562
Depth of pen.*Depth of pen.	1	0.6504	0.6504	3.83	0.057
2-Way Interaction	3	0.6377	0.2126	1.25	0.304
Cutting speed*Feed rate	1	0.1126	0.1126	0.66	0.420
Cutting speed*Depth of pen.	1	0.4475	0.4475	2.63	0.112
Feed rate*Depth of pen.	1	0.0777	0.0777	0.46	0.503
Error	41	6.9685	0.1700		
Lack-of-Fit	5	0.6278	0.1256	0.71	0.618
Pure Error	36	6.3407	0.1761		
Total	50	69.0662			

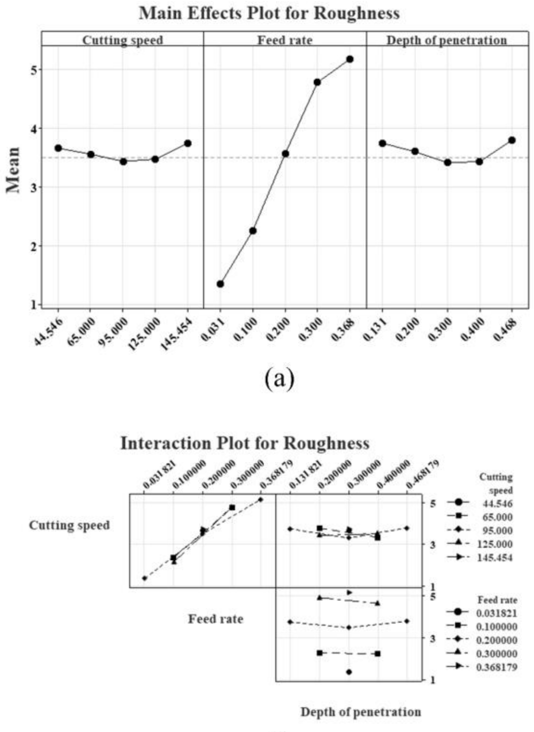

Fig. 7. Interaction and main effects plots of surface roughness (Ra) (a) main effects of individual parameters, and (b) interaction among cutting speed, feed rate, and penetration depth.

The lack-of-fit test was not significant ($p = 0.618$), confirming model adequacy. The model exhibited strong explanatory power, with $R^2 = 89.91\%$, adjusted $R^2 = 87.70\%$, and predicted $R^2 = 84.28$ (Table 10). The close agreement between adjusted and predicted R^2 values demonstrates reliable predictive capability, with approximately 90% of roughness variability explained by the selected factors.

Table 10. Model summary of surface roughness response.

S	R-sq	R-sq(adj)	R-sq(pred)
0.412266	89.91%	87.70%	84.28%

4.1.2. Surface Hardness (HV0.1)

Surface hardness values ranged from 133 HV0.1 (Run 13) to 276 HV0.1 (Run 25). Higher hardness values were consistently associated with greater penetration depths (0.3–0.4 mm), while shallow penetration depths produced values closer to the as-built baseline (190–240 HV0.1).

Residual plots (Fig 8) confirmed the validity of the regression model, showing normality ($p = 0.717$), random scatter of residuals versus fitted values, and independence in residuals versus order.

ANOVA results (Table 11) confirmed that the quadratic model was statistically significant ($p < 0.001$). Among the linear terms, penetration depth was dominant ($p < 0.001$), contributing the majority of explained variance (Sum of Squares = 66,146.7; F = 201.77). Cutting speed ($p = 0.242$) and feed rate ($p = 0.730$) had no significant influence at the 95% confidence level.

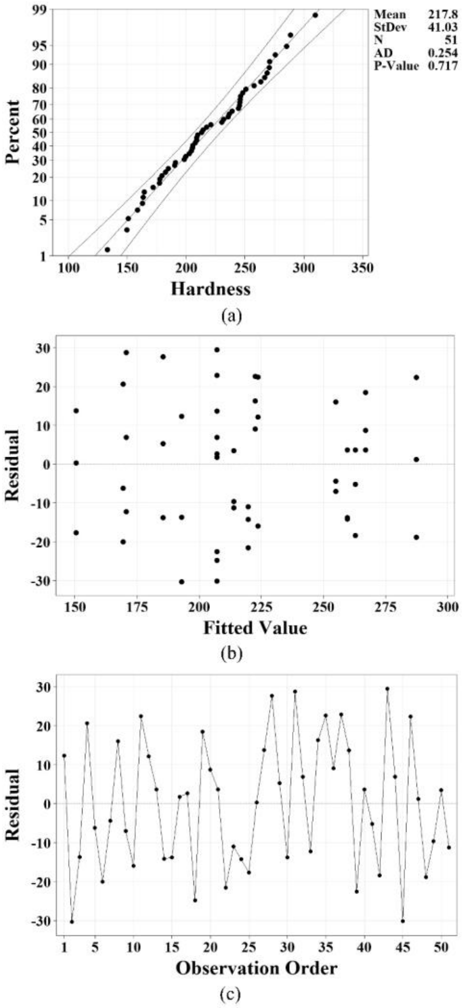

Fig 8. Statistical analysis of Hardness (a) Normal probability plot, (b) Residual versus fitted value, and (c) Residual versus order.

Quadratic and interaction terms contributed minimally. Only the interaction between cutting speed and penetration depth approached significance ($p = 0.078$), indicating a weak synergistic effect that did not reach statistical significance.

Table 11. Analysis of variance of surface hardness response.

Source	DF	Adj SS	Adj MS	F-Value	P-Value
Model	9	70714.4	7857.2	23.97	0.000
Linear	3	66648.7	22216.2	67.77	0.000
Cutting speed	1	462.3	462.3	1.41	0.242
Feed rate	1	39.7	39.7	0.12	0.730
Depth of penetration	1	66146.7	66146.7	201.77	0.000
Square	3	1250.1	416.7	1.27	0.297
Cutting speed*Cutting speed	1	565.2	565.2	1.72	0.196
Feed rate*Feed rate	1	820.2	820.2	2.50	0.121
Depth of pen.*Depth of pen.	1	584.9	584.9	1.78	0.189
2-Way Interaction	3	1203.7	401.2	1.22	0.313
Cutting speed*Feed rate	1	116.6	116.6	0.36	0.554
Cutting speed*Depth of pen.	1	1076.0	1076.0	3.28	0.077
Feed rate*Depth of pen.	1	11.1	11.1	0.03	0.855
Error	41	13440.9	327.8		
Lack-of-Fit	5	3020.5	604.1	2.09	0.090
Pure Error	36	10420.4	289.5		
Total	50	84155.3			

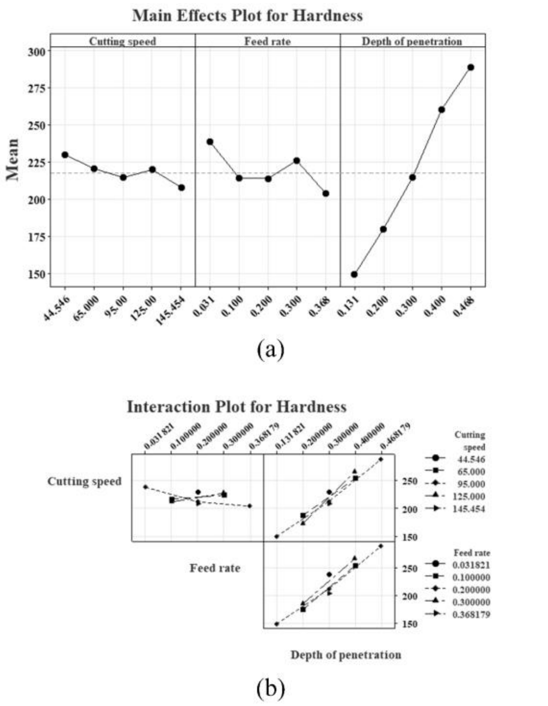

Fig 9. Interaction and main effects plots of surface hardness (HV0.1) (a) main effects of individual parameters., and (b) interaction among cutting speed, feed rate, and penetration depth.

The main and interaction effects in (Fig. 9) confirm these statistical findings. Penetration depth strongly increased hardness, whereas cutting speed and feed rate produced comparatively minor effects. The interaction between cutting speed and penetration depth showed weak coupling ($p = 0.078$), suggesting limited synergistic behavior that did not reach statistical significance.

The lack-of-fit test was not significant ($p = 0.090$), validating the model. The regression explained 84.03% of hardness variability (R^2 = 84.03%, adjusted R^2 = 80.52%, predicted R^2 = 75.65; (Table 12). The reasonable alignment between adjusted and predicted R^2 demonstrates robust model adequacy, though predictive capability for hardness was slightly lower than for roughness.

Table 12. Model summary of surface hardness response.

S	R-sq	R-sq(adj)	R-sq(pred)
18.1060	84.03%	80.52%	75.65%

In summary, the statistical evaluation confirmed that feed rate was the dominant factor influencing surface roughness ($p < 0.001$), while penetration depth was the dominant factor influencing surface hardness ($p < 0.001$). Cutting speed showed no significant effect within the tested range for either response. The regression models were statistically adequate, with R^2 values of 89.91% for roughness and 84.03% for hardness, supported by non-significant lack-of-fit tests and consistent residual diagnostics. These results demonstrate that the models can reliably predict surface responses across the design space.

4.2. Statistical optimization

4.2.1. Optimization

The multi-objective optimization was performed to minimize surface roughness while maximizing hardness. The response surface model identified the optimal parameter combination as:

- Cutting speed = 100.606 m·min^{-1}
- Feed rate = 0.0318 mm·rev^{-1}
- Depth of penetration = 0.468 mm

At these settings, the predicted responses were:

- Surface roughness (Ra) = 1.679 µm (95% CI: 0.945–2.413 µm)
- Hardness (HV0.1) = 301.9 HV0.1 (95% CI: 269.7–334.2 HV)

The composite desirability index was 0.9031, indicating strong overall adequacy in simultaneously achieving minimum surface roughness and maximum hardness (Fig. 10, Table 13).

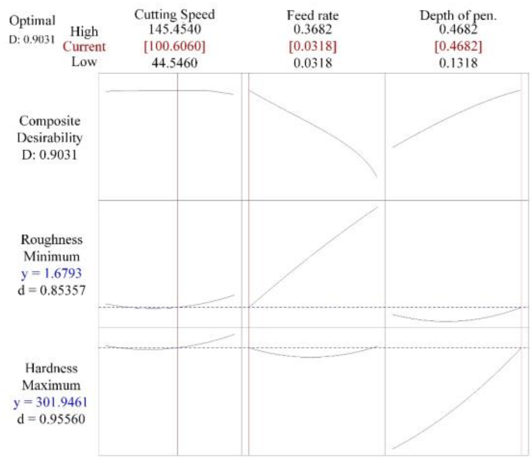

Fig. 10. Optimization results showing the composite desirability function for minimizing surface roughness and maximizing hardness.

Table 13. Multiple response prediction.

Variable				Setting
Cutting speed				100.606
Feed rate				0.0318207
Depth of penetration				0.468179
Response	**Fit**	**SE Fit**	**95% CI**	**95% PI**
Roughness	1.679	0.363	(0.945, 2.413)	(0.569, 2.789)
Hardness	301.9	16.0	(269.7, 334.2)	(253.2, 350.7)

4.2.2. Verification Trials

Experimental trials were carried out at the predicted optimum parameters to validate the model. The results (Table 14) showed:

- Average surface roughness (Ra) = 1.643 µm (SD = 0.032)
- Average hardness (HV0.1) = 308 HV0.1 (SD = 1.160)

These values were in excellent agreement with predictions (Ra = 1.679 µm; HV = 302 HV0.1) and fell within the 95% confidence intervals. The very low standard deviations confirmed process stability and repeatability. The strong correspondence between predicted and experimental outcomes demonstrates the reliability of the response surface methodology (RSM) framework for parameter selection.

Table 14. Experimental validation results at optimal parameters.

Trial Run	Surface Roughness, Ra (µm)	Surface Hardness (HV0.1)
1	1.642	309
2	1.671	307
3	1.598	308
4	1.653	310
5	1.615	309
6	1.688	307
7	1.623	308
8	1.674	307
9	1.602	310
10	1.659	308
Average	1.643	308
SD.	0.032	1.160

Overall, the optimization confirmed that a low feed rate, high penetration depth, and moderate cutting speed produced the best balance between reduced roughness and enhanced hardness. The verification trials validated the predictive accuracy and repeatability of the model, confirming its suitability for process optimization.

4.3. Microstructural Analysis

4.3.1. Porosity Analysis

The relative density of the BMD-produced 316L stainless steel specimens was evaluated by image-based porosity quantification. Longitudinal cross-sections (Fig. 11) revealed distributed voids located between deposited layers, consistent with the layer-by-layer deposition process. Five embossing locations were analyzed to ensure representative coverage.

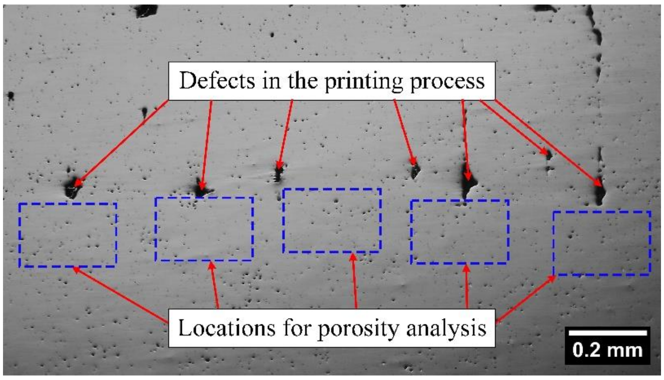

Fig. 11. Defect characteristics and porosity locations in BMD-produced 316L stainless steel. Longitudinal section reveals layer-related voids distributed across multiple tracks

ImageJ processing (Fig. 12) was used to threshold grayscale micrographs and convert them into binary images for quantitative pore fraction measurement. The overlays confirmed that pores were present both within grains and along grain boundaries.

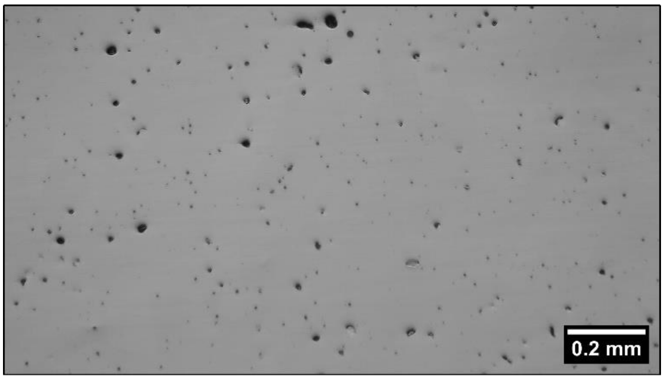

(a)

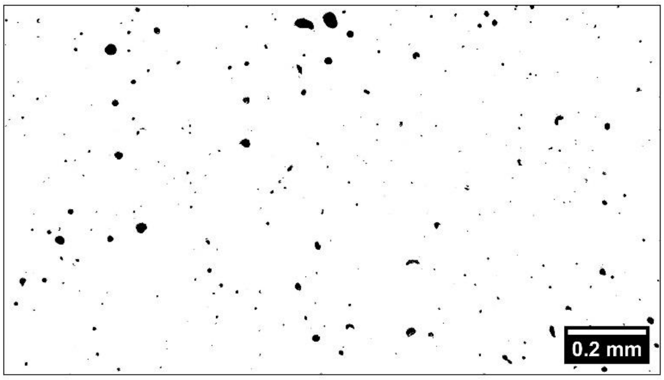

(b)

Fig. 12. Image analysis procedure for porosity evaluation in BMD-produced 316L stainless steel. (a) Thresholding of grayscale micrograph to isolate pores; (b) binary conversion for quantitative measurement, showing pore area fraction used for density calculations.

Quantitative results are summarized in Table 15. The relative densities ranged from 98.25% to 98.61%, with an overall average of 98.46%. This indicates a high degree of densification, though small residual pores remained.

Table 15. Quantitative porosity analysis results of BMD-produced 316L stainless steel specimens. Relative densities range from 98.25% to 98.61% with an overall average of 98.46%, confirming high densification but persistence of localized pores that may serve as crack initiation sites.

Measured Position	Relative Density (%)
1	98.42
2	98.49
3	98.25
4	98.52
5	98.61
Average	98.46

The analysis confirmed that the BMD specimens achieved consistently high relative densities, with only localized porosity remaining. These results provide the basis for examining how roller burnishing modifies the near-surface microstructure.

4.3.2. Microstructural changes

Optical microscopy revealed that roller burnishing modified the surface morphology of the BMD 316L specimens. In the as-built condition, the surface exhibited visible asperities and pore openings. After burnishing, asperities were flattened, near-surface pores were partially closed, and material flow was observed along the burnishing direction (Fig. 13).

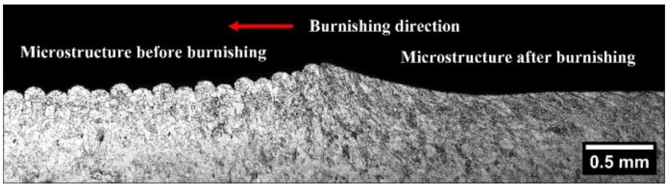

Fig. 13. Microstructural evolution of BMD 316L stainless steel before and after roller burnishing. Burnished surface shows flattened asperities, partial pore closure (arrows), and material flow along the roller direction, confirming densification and plastic deformation in the near-surface region.

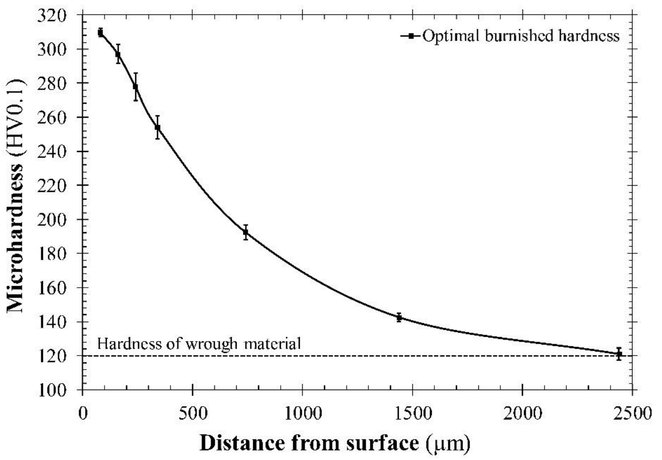

Fig. 14. Hardness–depth profile of burnished BMD 316L specimen. Surface hardness increased to >300 HV0.1 (compared to ~110 HV0.1 bulk), with a hardened case depth of ~1.0–1.2 mm, validating strain hardening and densification in the plastically deformed zone

The hardness–depth profile (Fig. 14) confirmed the presence of a hardened case layer. Surface hardness increased to values above 300 HV0.1, compared to the bulk hardness of approximately 110 HV0.1. Hardness gradually decreased with depth and stabilized beyond 1.0–1.2 mm, defining the effective case depth.

Crack-related features were also observed, as shown in (Fig. 15), where cracks were already present in the as-built BMD specimen before burnishing. These cracks originated from residual porosity and particle-boundary defects generated during the printing process, highlighting the inherent defect sensitivity of BMD alloys.

In contrast, (Fig. 16) corresponds to a repeat verification test conducted under the optimized parameters (Vc ≈ 100.6 $m \cdot min^{-1}$, f = 0.0318 $mm \cdot rev^{-1}$, depth = 0.468 mm; Trial Run 4, Ra = 1.653 μm, HV = 310). The specimen was examined for microstructural analysis, and localized cracks were again detected at printing-induced defects, where stress concentrations remained high despite overall surface improvement. These cracks were shallow, sporadic, and did not affect the averaged Ra (1.643 μm) or HV (308) obtained under the optimum condition.

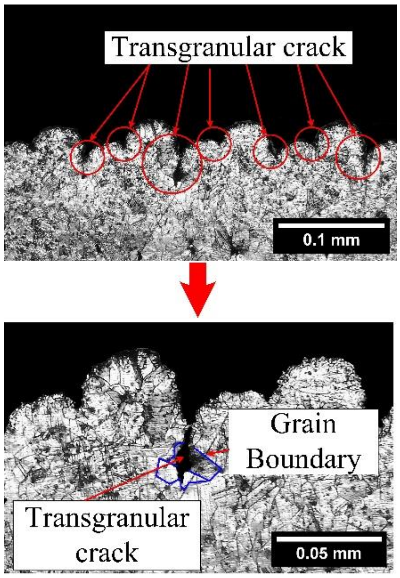

Fig. 15. Crack initiation in roller-burnished BMD 316L stainless steel. Cracks initiate transgranularly at asperity peaks and near-surface pores (arrows), where local stress concentrations are highest due to incomplete surface smoothing.

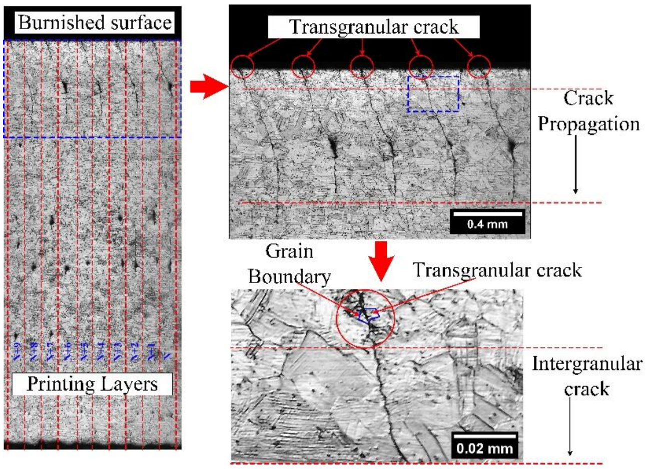

Fig. 16. Crack propagation in roller-burnished BMD 316L stainless steel. Cracks deflect along grain boundaries, prior particle boundaries, and sintering oxides, transitioning from transgranular to intergranular fracture paths.

These results confirm that roller burnishing effectively produced a hardened case layer of approximately 1.0–1.2 mm, accompanied by partial pore closure and strain hardening. The cracks documented in Fig. 15 and Fig. 16 were linked to printing-related porosity rather than process-induced defects, emphasizing that BMD materials inherently contain defects that can occasionally act as crack initiation sites. While RB improved surface integrity overall, such defects may still influence fatigue and corrosion resistance and should be considered in future studies.

4.3.3. Electron Backscatter Diffraction (EBSD) Analysis

EBSD mapping provided further insight into the microstructural condition of the BMD 316L specimens before and after roller burnishing (Fig. 17).

Inverse Pole Figure (IPF) maps showed equiaxed grains with random orientations in the as-built state (Fig. 17a). After burnishing (Fig. 17b), the near-surface grains exhibited elongation and orientation alignment along the burnishing direction.

Phase maps (Fig. 17c–d) confirmed that the material remained fully austenitic before and after processing, with no evidence of martensitic or ferritic transformation. The burnished sample exhibited localized heterogeneities near the surface but retained its austenitic structure.

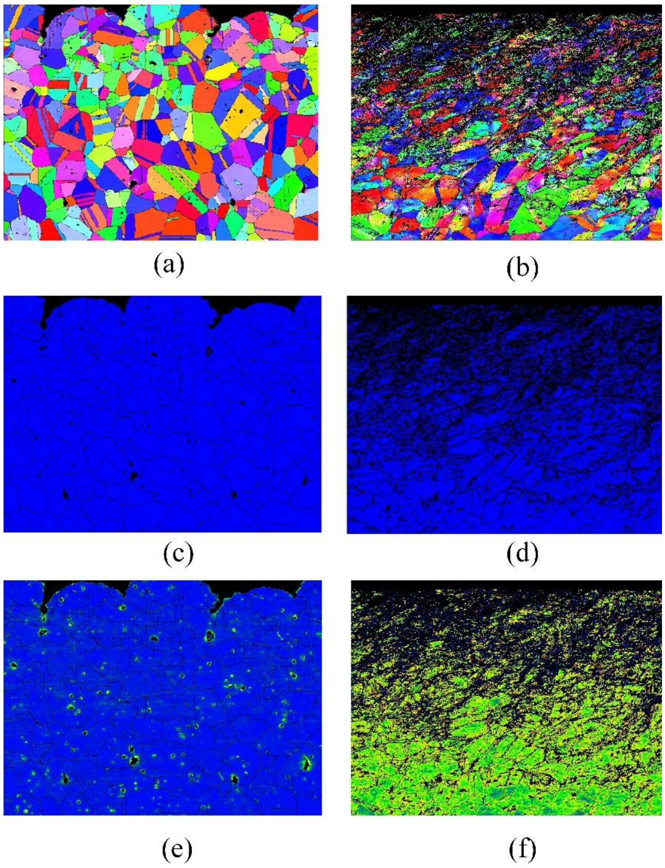

Fig. 17. EBSD maps of BMD 316L stainless steel before and after roller burnishing. (a, c, f) As-built state: equiaxed grains, fully austenitic phase, low KAM values; (b, d, g) Burnished state: elongated grains, localized lattice distortion, and higher KAM near the surface, confirming grain refinement and increased dislocation density.

Kernel Average Misorientation (KAM) maps (Fig. 17e-f) revealed low misorientation values in the as-built state (mean = 0.12°). In contrast, the burnished condition showed higher misorientation within the first few hundred micrometers from the surface, with a mean of 1.25°. This indicates a substantial increase in lattice curvature.

Quantitative EBSD analysis (Fig. 18) confirmed these observations. Grain size distribution shifted from an average equivalent diameter of 21.36 µm in the as-built state (Fig. 18c) to 15.43 µm in the burnished state (Fig. 18d). KAM distributions also broadened after burnishing, with the frequency of higher misorientation values increasing substantially (Fig. 18a–b).

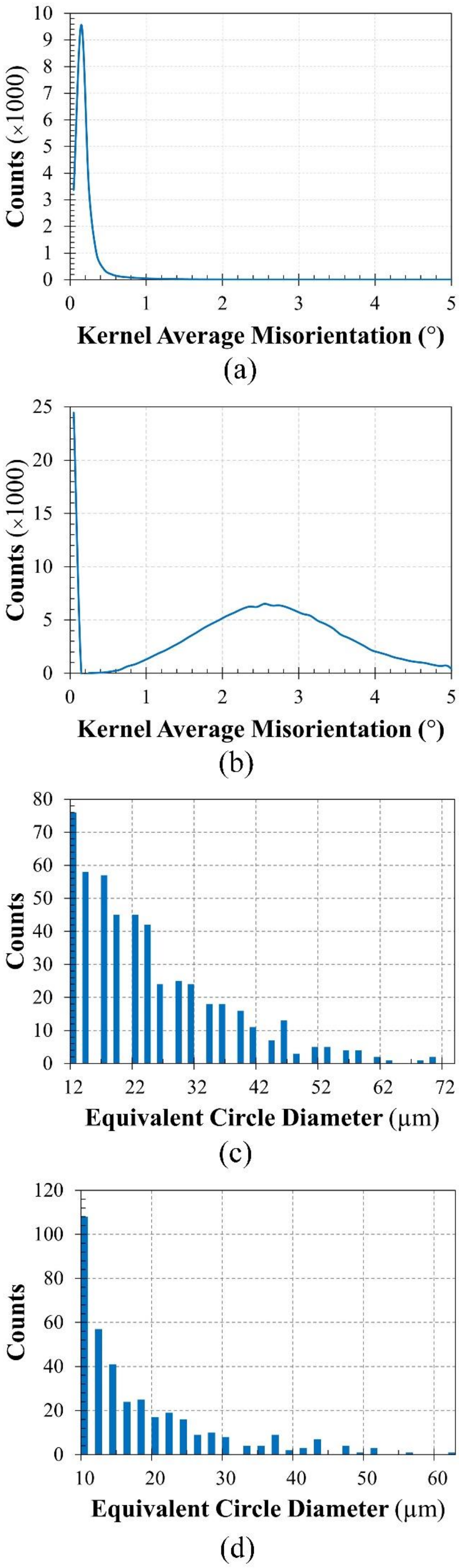

Fig. 18. Quantitative EBSD analysis of BMD 316L stainless steel before and after roller burnishing. (a–b) KAM distributions: mean value increased from 0.12° (as-built) to 1.25° (burnished), confirming higher dislocation density. (c–d) Grain size distributions: average grain size reduced from ~21.36 μm to ~15.43 μm, demonstrating refinement via sub-grain formation.

Overall, EBSD analysis confirmed that roller burnishing refined the near-surface grains, increased local misorientation, and introduced measurable substructures while maintaining a fully austenitic phase composition. These findings provide the crystallographic evidence to complement the hardness–depth profile and microstructural observations presented in Sections 4.3.1 and 4.3.2.

4.4. Integrated Interpretation

The results presented in Sections 4.1–4.3 provide complementary insights into the effects of roller burnishing on BMD-fabricated 316L stainless steel. The statistical models identified feed rate as the dominant factor controlling surface roughness, while penetration depth governed hardness. Cutting speed showed negligible influence within the tested range. Microstructural and EBSD analyses confirmed that these macroscopic outcomes were underpinned by asperity deformation, pore closure, strain hardening, and grain refinement in the near-surface region. These mechanisms, in turn, carry important implications for fatigue and wear behavior, though direct validation is still required.

4.4.1. Surface Roughness and Asperity Deformation

The statistical analysis (Section 4.1.1) demonstrated that feed rate contributed nearly 90% of the variability in surface roughness. This outcome is consistent with asperity deformation: lower feed rates promote stable plastic flow and smoothing, whereas higher feed rates induce ploughing and surface tearing. Similar trends have been reported in both AM and conventionally machined steels, where feed rate was consistently the most sensitive parameter for surface finish (Revankar et al., 2017; Rotella et al., 2020; Somatkar et al., 2024). For BMD, staircase asperities arising from extrusion-based deposition make feed rate control particularly critical. A ~95% reduction in Ra (from 21.3 μm to 1.643 μm) is expected to significantly delay fatigue crack initiation by eliminating surface stress concentrators, as observed in LPBF steels where smoother surfaces led to >10× improvements in fatigue life (Davoodi et al., 2023; Sayadi et al., 2023).

The comparison between BMD and LPBF/LDED alloys is essential to clarify the distinct strengthening mechanisms activated during roller burnishing. In LPBF and LDED systems, surface integrity improvements are mainly attributed to redistribution of residual stresses, refinement of melt-pool microstructures, and reduction of defect sensitivity through localized re-solidification (Duncheva et al., 2024; Liu et al., 2024; Maximov et al., 2024). By contrast, BMD components exhibit sintering-induced porosity and coarser grain structures, which require a different strengthening route. In BMD, improvements are achieved primarily through closure of residual pores and strain hardening of the sintered microstructure, both of which demand a greater depth of penetration during burnishing to generate sufficient plastic deformation for pore suppression. Therefore, the burnishing parameters effective for LPBF/DED alloys cannot be directly transferred to BMD, highlighting the need for process optimization tailored to its unique densification and work-hardening behavior.

4.4.2. Hardness and Strain Hardening Mechanisms

Section 4.1.2 confirmed that penetration depth was the sole statistically significant factor influencing hardness ($p < 0.001$). This reflects its role as a surrogate for applied pressure: deeper penetration induces greater plastic deformation, increasing dislocation density and promoting pore closure. EBSD results (Section 4.3.3) corroborated this finding, showing an increase in Kernel Average Misorientation from 0.12° to 1.25° and grain size refinement from 21.36 μm to 15.43 μm. These crystallographic modifications are characteristic of Hall–Petch strengthening and confirm that hardness improvements arise from work hardening rather than phase transformation (Revankar et al., 2017; Rotella et al., 2020; Sayadi et al., 2023).

The >2× hardness increase (>300 HV vs. 129 HV as-built) suggests improved wear resistance and crack growth retardation, although dedicated tribological testing is still required. Crack features were also documented. Micrographs showed transgranular initiation at asperity peaks and near-surface pores, followed by propagation into the subsurface (Fig. 15). At greater depths, cracks deflected along grain boundaries, prior particle boundaries, and sintering oxides, producing intergranular fracture paths (Fig. 16).

In the present study, roller burnishing was shown to partially mitigate the intrinsic defects of BMD materials described by Basak et al. (2024). The applied contact pressure and localized plastic deformation promoted the closure of near-surface pores, reducing the effective porosity and homogenizing the surface layer. Concurrently, strain hardening enhanced hardness and reduced the anisotropy of surface mechanical responses. Compared with the as-built condition, burnished BMD 316L exhibited both lower surface roughness and higher uniformity in hardness distribution, indicating that RB can serve as a simple yet effective post-processing step to compensate for the density deficit and anisotropy inherent to BMD steels.

4.4.3. Porosity and Crack Behavior

Porosity measurements (Section 4.3.1) indicated high bulk relative densities (98.25–98.61%), yet residual pores persisted near grain boundaries. Roller burnishing was effective in closing surface-connected pores within the hardened case depth (~1.0–1.2 mm). This localized densification explains the observed delay in crack initiation, as surface pores often act as stress concentrators. Nevertheless, micrographs (**Fig. 15–Fig. 16**) revealed that cracks could still initiate transgranularly at asperity peaks and transition into intergranular paths along grain boundaries and sintering oxides, in line with previous findings in AM stainless steels (Gumma et al., 2025; Maximov et al., 2024). For BMD, pore closure offers an additional fatigue-resistance mechanism absent in LPBF alloys, though direct fatigue testing must confirm this hypothesis.

4.4.4. BMD versus LPBF Response

A key contribution of this study lies in differentiating the response of BMD stainless steel from that of laser-based AM alloys. In LPBF 316L, roller burnishing primarily modifies melt-pool solidification patterns and redistributes residual stresses (Davoodi et al., 2023; Sayadi et al., 2023). By contrast, in BMD, improvements arise from pore closure, asperity deformation, and strain hardening of a coarser, sintered microstructure. This distinction underscores the novelty of the present work: optimization of roller burnishing parameters for BMD cannot simply be extrapolated from LPBF studies. This distinction underscores the novelty of the present work. However, extrapolation from LPBF to BMD in terms of fatigue improvement remains speculative until validated experimentally.

4.4.5. Operational Implications

From a production engineering perspective, the findings provide actionable guidance for process planning. Feed rate must be tightly controlled to achieve Ra < 1 μm, while penetration depth is a reliable surrogate for applied pressure in achieving surface hardening. Cutting speed was statistically insignificant, simplifying parameter selection and reducing optimization requirements. The validated RSM framework (Section 4.2) provides a predictive tool with desirability above 0.90, enabling consistent outcomes.

For industry, this translates into smoother surfaces and hardened layers without expensive thermal or chemical post-processing. Roller burnishing thus emerges as a cost-effective, geometry-preserving finishing method for BMD components. Nevertheless, it must be emphasized that fatigue, wear, and corrosion tests were not performed in this study. While the microstructural evidence strongly suggests enhanced durability, future work must quantify life extension before claims of aerospace, biomedical, or tooling deployment can be substantiated.

5. Summary and conclusion

This study systematically optimized roller burnishing for BMD-fabricated AISI 316L stainless steel, establishing quantitative relationships between process parameters, surface integrity, and microstructural evolution. Response Surface Methodology (RSM) confirmed that feed rate was the dominant factor controlling surface roughness, while penetration depth primarily governed hardness. Cutting speed showed no measurable influence within the tested range.

At optimal parameters (cutting speed = 100.6 $m \cdot min^{-1}$, feed rate = 0.032 $mm \cdot rev^{-1}$, penetration depth = 0.468 mm), surface roughness decreased from 21.3 μm in the as-built condition (Table 4) to 1.643 μm (verification, Table 14), representing a ~95 % reduction. Hardness simultaneously increased from 129 HV0.1 (as-built, Table 4) to 308 HV0.1 (verification, Table 14), corresponding to a more than two-fold improvement. Averaged data across all experimental conditions (Table 8) further showed maximum hardness of ~289 HV0.1 and typical ΔRa values of 16–20 μm, confirming that feed rate control critically affects roughness, while deeper penetration produces markedly higher hardness within a hardened case depth of approximately 1.0–1.2 mm.

Microstructural and EBSD analyses provided mechanistic explanations for these macroscopic outcomes. Improvements were driven by asperity deformation, partial pore closure, strain hardening, and grain refinement, with average grain size reduced from 21.36 µm (as-built) to 15.43 µm after burnishing. Kernel Average Misorientation increased from 0.12° to 1.25°, confirming higher dislocation density consistent with Hall–Petch strengthening.

From an operational perspective, roller burnishing offers a cost-effective, geometry-preserving post-processing method for BMD stainless steels. While the findings highlight potential relevance for aerospace, biomedical, and tooling applications, further validation through fatigue, wear, and corrosion testing is necessary before deployment in service-critical environments.

Limitations of this work include reliance on a single BMD production batch, the use of penetration depth as a surrogate for contact pressure, and the absence of fatigue data.

Future work should expand the quantitative EBSD characterization by including additional 3D metrics such as grain aspect ratio, orientation spread, and boundary misorientation statistics to better capture deformation-induced anisotropy. Complementary functional testing – such as fatigue, wear, or corrosion evaluation – would also strengthen the correlation between microstructural refinement and service performance. In addition, comparisons with recent SRB and UR studies on LPBF/DED 316L alloys (Duncheva et al., 2024; Liu et al., 2024; Maximov et al., 2024) could provide valuable benchmarks for understanding the extent to which the pore-closure–dominated mechanisms of BMD differ from melt-pool–refinement mechanisms in fusion-based AM systems.

Overall, this study establishes the first predictive, experimentally validated framework for roller burnishing of BMD 316L, providing both quantitative optimization and mechanistic insights that expand post-processing knowledge for binder-based AM technologies.

Acknowledgements

The authors gratefully acknowledge the Department of Industrial Engineering, Faculty of Engineering, Rajamangala University of Technology Thanyaburi (RMUTT) for providing essential academic support and research facilities that enabled the successful completion of this study. The authors also extend their appreciation to the Mechanical Technology Department, Inburi Industrial and Community Education College, for their technical assistance and valuable collaboration during the experimental work.

References

Afkhami, S., Dabiri, M., Piili, H., & Björk, T., 2021. Effects of manufacturing parameters and mechanical post-processing on stainless steel 316L processed by laser powder bed fusion. Materials Science and Engineering: A, 802. DOI: 10.1016/j.msea.2020.140660

Alemdar, A. S., & Gardi, R., 2018. Effect of roller burnishing tool pass on surface roughness of austenitic stainless steel AISI 316L. Zanco Journal of Pure and Applied Sciences, 29, 7. DOI: 10.21271/ZJPAS.29.6.9

Armstrong, M., Mehrabi, H., & Naveed, N., 2022. An overview of modern metal additive manufacturing technology. Journal of Manufacturing Processes, 84, 1001-1029. DOI: 10.1016/j.jmapro.2022.10.060

Basak, A. K., Pramanik, A., Chen, Y. X., Prakash, C., Radhika, N., & Shankar, S., 2024. Bound metal deposition of stainless steel 316L: Effect of process variables on microstructural and mechanical behaviors. Materialia, 36, 102196. DOI: 10.1016/j.mtla.2024.102196

Bello, K. A., Kanakana-Katumba, M. G., & Maladzhi, R. W., 2023. A Review of Additive Manufacturing Post-Treatment Techniques for Surface Quality Enhancement. Procedia CIRP, 120, 404-409. DOI: 10.1016/j.procir.2023.09.010

Bobrovskij, I., Bobrovskij, N., Khaimovich, A., & Travieso-Rodriguez, J. A., 2022. Impacts of Surface Texture and Nature of Friction on Energy-Force Efficiency of Surface Plastic Deformation during Burnishing. Metals, 12(10). DOI: 10.3390/met12101568

Boudjerada, A., & Ghochi, M., 2024. Experimental study of the impact of burnishing parameters on the quality of machined surface finish. Universite kasdi merbah ouargla,

Cobanoglu, T., & Ozturk, S., 2014. Effect of burnishing parameters on the surface quality and hardness. Proceedings of the Institution of Mechanical Engineers, Part B: Journal of Engineering Manufacture, 229(2), 286-294. DOI: 10.1177/0954405414527962

D'Andrea, D., 2023. Additive Manufacturing of AISI 316L Stainless Steel: A Review. Metals, 13(8). DOI: 10.3390/met13081370

Davoodi, F., Taghian, M., Carbone, G., Saboori, A., & Iuliano, L., 2023. An Overview of the Latest Progress in Internal Surface Finishing of the Additively Manufactured Metallic Components. Materials, 16(10). DOI: 10.3390/ma16103867

Duncheva, G., Maximov, J., Anchev, A., Dunchev, V., Anastasov, K., & Argirov, Y., 2024. Effect of Roller Burnishing and Slide Roller Burnishing on Fatigue Strength of AISI 304 Steel: Comparative Analysis. Metals, 14(6). DOI: 10.3390/met14060710

El-Khabeery, M. M., & El-Axir, M. H., 2001. Experimental techniques for studying the effects of milling roller-burnishing parameters on surface integrity. International Journal of Machine Tools and Manufacture, 41(12), 1705-1719. DOI: 10.1016/s0890-6955(01)00036-0

Ferencsik, V., 2023. Analytical analysis of the theoretical surface roughness in the case of burnishing of cylindrical workpiece. Cutting & Tools in Technological System(99), 101-109.

Ford, S., & Despeisse, M., 2016. Additive manufacturing and sustainability: an exploratory study of the advantages and challenges. Journal of Cleaner Production, 137, 1573-1587. DOI: 10.1016/j.jclepro.2016.04.150

Frazier, W. E., 2014. Metal Additive Manufacturing: A Review. Journal of Materials Engineering and Performance, 23(6), 1917-1928. DOI: 10.1007/s11665-014-0958-z

Gabilondo, M., Cearsolo, X., Arrue, M., & Castro, F., 2022. Influence of Build Orientation, Chamber Temperature and Infill Pattern on Mechanical Properties of 316L Parts Manufactured by Bound Metal Deposition. Materials, 15(3). DOI: 10.3390/ma15031183

Gao, W., Zhang, Y., Ramanujan, D., Ramani, K., Chen, Y., Williams, C. B., . . . Zavattieri, P. D., 2015. The status, challenges, and future of additive manufacturing in engineering. Computer-Aided Design, 69, 65-89. DOI: 10.1016/j.cad.2015.04.001

Ge, J., Pillay, S., & Ning, H., 2023. Post-Process Treatments for Additive-Manufactured Metallic Structures: A Comprehensive Review. Journal of Materials Engineering and Performance, 32(16), 7073-7122. DOI: 10.1007/s11665-023-08051-9

Gonzalez-Gutierrez, J., Cano, S., Schuschnigg, S., Kukla, C., Sapkota, J., & Holzer, C., 2018. Additive Manufacturing of Metallic and Ceramic Components by the Material Extrusion of Highly-Filled Polymers: A Review and Future Perspectives. Materials, 11(5). DOI: 10.3390/ma11050840

Grudzień, J., Grochała, D., Grzejda, R., & Kochmański, P., 2024. Testing the Effectiveness of Hybrid Milling and Surface Burnishing in Improving the Wear Resistance of Machine Parts Made of Structural Steel. Lubricants, 12(12). DOI: 10.3390/lubricants12120458

Gumma, S., Swami, M. K., Reddy, G. B., Ganesh, P., Donthula, H., Rai, S. K., & Roychowdhury, S., 2025. Controlled Surface Rolling: A Novel Low Plasticity Burnishing Technique to Mitigate Stress Corrosion Cracking in Machined SS304L. Journal of Materials Engineering and Performance, 34(12), 11101-11118. DOI: 10.1007/s11665-025-10921-3

Kalisz, J., Żak, K., Wojciechowski, S., Gupta, M. K., & Krolczyk, G. M., 2021. Technological and tribological aspects of milling-burnishing process of complex surfaces. Tribology International, 155, 106770. DOI: 10.1016/j.triboint.2020.106770

Karthick Raaj, R., Vijay Anirudh, P., Karunakaran, C., Kannan, C., Jahagirdar, A., Joshi, S., & Balan, A. S. S., 2020. Exploring grinding and burnishing as surface post-treatment options for electron beam additive manufactured Alloy 718. Surface and Coatings Technology, 397, 126063. DOI: 10.1016/j.surfcoat.2020.126063

Kedziora, S., Decker, T., Museyibov, E., Morbach, J., Hohmann, S., Huwer, A., & Wahl, M., 2022. Strength Properties of 316L and 17-4 PH Stainless

Steel Produced with Additive Manufacturing. Materials, 15(18). doi:10.3390/ma15186278
Kumar, N., Sachdeva, A., Singh, L. P., & Tripathi, H., 2016. Experimental investigation of effect of roller burnishing process parameters on surface roughness and surface hardness of C40E steel. International Journal of Machining and Machinability of Materials, 18(1-2), 185-199.
Kurdi, A., Tabbakh, T., & Basak, A. K., 2023. Microstructural and Nanoindentation Investigation on the Laser Powder Bed Fusion Stainless Steel 316L. Materials, 16(17). DOI: 10.3390/ma16175933
Li, F. L., Xia, W., Zhou, Z. Y., Zhao, J., & Tang, Z. Q., 2012. Analytical prediction and experimental verification of surface roughness during the burnishing process. International Journal of Machine Tools and Manufacture, 62, 67-75. DOI: 10.1016/j.ijmachtools.2012.06.001
Liu, G., Su, Y., Pi, X., Liu, D., & Lin, Y., 2024. Fatigue Strength Improvement of Laser-Directed Energy Deposition 316L Stainless Steel with In Situ Ultrasonic Rolling by Preliminary Investigation. Materials, 17(15). DOI: 10.3390/ma17153693
Low, K. O., & Wong, K. J., 2011. Influence of ball burnishing on surface quality and tribological characteristics of polymers under dry sliding conditions. Tribology International, 44(2), 144-153. DOI: 10.1016/j.triboint.2010.10.005
Malakizadi, A., Mallipeddi, D., Dadbakhsh, S., M'Saoubi, R., & Krajnik, P., 2022. Post-processing of additively manufactured metallic alloys – A review. International Journal of Machine Tools and Manufacture, 179, 103908. DOI: 10.1016/j.ijmachtools.2022.103908
Maximov, J., Duncheva, G., Anchev, A., Dunchev, V., Anastasov, K., & Daskalova, P., 2024. Effect of Roller Burnishing and Slide Roller Burnishing on Surface Integrity of AISI 316 Steel: Theoretical and Experimental Comparative Analysis. Machines, 12(1). DOI: 10.3390/machines12010051
Ngo, T. D., Kashani, A., Imbalzano, G., Nguyen, K. T. Q., & Hui, D., 2018. Additive manufacturing (3D printing): A review of materials, methods, applications and challenges. Composites Part B: Engineering, 143, 172-196. DOI: 10.1016/j.compositesb.2018.02.012
Nguyen, T.-T., Minh, T.-L., Chung, T.-N., Nguyen, T.-A., Van, Q.-N., Bui, H.-T., Le, L.-V., 2024. Assessments of energy efficiency of the green mql-assisted multi-roller burnishing process.
Noronha, D. J., Sharma, S., Prabhu Parkala, R., Shankar, G., Kumar, N., & Doddapaneni, S., 2024. Deep Rolling Techniques: A Comprehensive Review of Process Parameters and Impacts on the Material Properties of Commercial Steels. Metals, 14(6). DOI: 10.3390/met14060667
Okuniewski, W., Walczak, M., & Szala, M., 2024. Effects of Shot Peening and Electropolishing Treatment on the Properties of Additively and Conventionally Manufactured Ti6Al4V Alloy: A Review. Materials, 17(4). DOI: 10.3390/ma17040934
Priyadarsini, C., Venkata Ramana, V. S. N., Aruna Prabha, K., & Swetha, S., 2019. A Review on Ball, Roller, Low Plasticity Burnishing Process. Materials Today: Proceedings, 18, 5087-5099. DOI: 10.1016/j.matpr.2019.07.505
Revankar, G. D., Shetty, R., Rao, S. S., & Gaitonde, V. N., 2017. Wear resistance enhancement of titanium alloy (Ti–6Al–4V) by ball burnishing process. Journal of Materials Research and Technology, 6(1), 13-32. DOI: 10.1016/j.jmrt.2016.03.007
Rodriguez, A., de Lacalle, L. N. L., Pereira, O., Fernandez, A., & Ayesta, I., 2020. Isotropic finishing of austempered iron casting cylindrical parts by roller burnishing. Int J Adv Manuf Technol, 110(3-4), 753-761. DOI: 10.1007/s00170-020-05894-7
Rotella, G., Filice, L., & Micari, F., 2020. Improving surface integrity of additively manufactured GP1 stainless steel by roller burnishing. CIRP Annals, 69(1), 513-516. DOI: 10.1016/j.cirp.2020.04.015
Saboori, A., Aversa, A., Marchese, G., Biamino, S., Lombardi, M., & Fino, P., 2020. Microstructure and Mechanical Properties of AISI 316L Produced by Directed Energy Deposition-Based Additive Manufacturing: A Review. Applied Sciences, 10(9). DOI: 10.3390/app10093310
Sanguedolce, M., Rotella, G., Saffioti, M. R., & Filice, L., 2022. Burnishing of AM materials to obtain high performance part surfaces. Journal of Industrial Engineering and Management, 15(1), 92. DOI: 10.3926/jiem.3608
Sayadi, D., Rangrizian, H., Khodabandeh, A., Nezarati, M., Hemasian Etefagh, A., Khajehzadeh, M., & Razfar, M. R., 2023. Using shot peening and burnishing to improve fatigue performance of additively manufactured 316L stainless steel. Proceedings of the Institution of Mechanical Engineers, Part L: Journal of Materials: Design and Applications, 238(4), 707-722. DOI: 10.1177/14644207231196266
Somatkar, A. A., Dwivedi, R., & Chinchanikar, S. S., 2024. Enhancing surface integrity and quality through roller burnishing: a comprehensive review of parameters optimization, and applications. Communications on Applied Nonlinear Analysis, 31(1s), 151-169.
Teimouri, R., & Amini, S., 2019. Analytical modeling of ultrasonic surface burnishing process: Evaluation of through depth localized strain. International Journal of Mechanical Sciences, 151, 118-132. DOI: 10.1016/j.ijmecsci.2018.11.008
Teschke, M., Moritz, J., Tenkamp, J., Marquardt, A., Leyens, C., & Walther, F., 2022. Defect-based characterization of the fatigue behavior of additively manufactured titanium aluminides. International Journal of Fatigue, 163, 107047. DOI: 10.1016/j.ijfatigue.2022.107047
Vukelic, D., Miljanić, D., Randjelović, S., Budak, I., Dzunic, D., Erić, M., & Pantić, M., 2013. Burnishing process based on the optimal depth of workpiece penetration.
Xiang, F., Zhao, Y., Zhang, M., Zuo, Y., Zou, X., & Tao, F., 2024. Ensemble learning-based stability improvement method for feature selection towards performance prediction. Journal of Manufacturing Systems, 74, 55-67. DOI: 10.1016/j.jmsy.2024.03.001
Yildiz, R. A., Ozdogan, C., & Malekan, M., 2024. On the surface roughness of 316L stainless steel fabricated using L-PBF additive, 41.